

Aerosol-Assisted CVD-Grown WO₃ Nanoneedles Decorated with Copper Oxide Nanoparticles for the Selective and Humidity-Resilient Detection of H₂S

Fatima E. Annanouch,[†] Zouhair Haddi,[†] Stella Vallejos,^{‡,§} Polona Umek,[⊥] Peter Guttman,^{||} Carla Bittencourt,[#] and Eduard Llobet^{*,†}

[†]Research Centre on the Engineering of Materials and micro/nano Systems, Universitat Rovira i Virgili Països Catalans 26, 43007 Tarragona, Spain

[‡]SIX Research Center, Faculty of Electrical Engineering and Communication, Brno University of Technology, Technická 12, CZ-61600 Brno, Czech Republic

[§]Instituto de Microelectrónica de Barcelona, Consejo Superior de Investigaciones Científicas, Campus UAB, 08193 Bellaterra, Barcelona, Spain

[⊥]Solid State, Physics Department, Jožef Stefan Institute, 39 Jamova cesta, 1000 Ljubljana, Slovenia

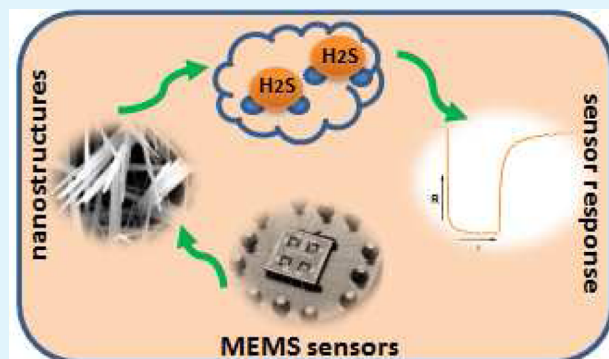
^{||}Helmholtz-Zentrum Berlin für Materialien und Energie GmbH, Institute for Soft Matter and Functional Materials, Albert-Einstein-Strasse 15, 12489 Berlin, Germany

[#]Plasma-Surface Interaction Chemistry University of Mons, 1 Copernic, 7000 Mons, Belgium

Supporting Information

ABSTRACT: A gas-sensitive hybrid material consisting of Cu₂O nanoparticle-decorated WO₃ nanoneedles is successfully grown for the first time in a single step via aerosol-assisted chemical vapor deposition. Morphological, structural, and composition analyses show that our method is effective for growing single-crystalline, n-type WO₃ nanoneedles decorated with p-type Cu₂O nanoparticles at moderate temperatures (i.e., 380 °C), with cost effectiveness and short fabrication times, directly onto microhot plate transducer arrays with the view of obtaining gas sensors. The gas-sensing studies performed show that this hybrid nanomaterial has excellent sensitivity and selectivity to hydrogen sulfide (7-fold increase in response compared with that of pristine WO₃ nanoneedles) and a low detection limit (below 300 ppb of H₂S), together with unprecedented fast response times (2 s) and high immunity to changes in the background humidity. These superior properties arise because of the multiple p–n heterojunctions created at the nanoscale in our hybrid nanomaterial.

KEYWORDS: aerosol-assisted CVD, nanoneedles, nanoparticles, functionalization, gas sensor



INTRODUCTION

Hydrogen sulfide (H₂S) is a colorless, flammable, and very poisonous gas with a characteristic smell of rotten eggs. It can be released from sewage, manure, hot springs, and food processing.^{1–3} The acceptable ambient limit for H₂S (recommended by the Scientific Advisory Board on Toxic Air Pollutants, USA) is in the range of 20–100 ppb,^{4–7} while the typical permissible exposure limit of this gas according to the U.S. Occupational Safety and Health Administration is about 10 ppm.^{8–10} People exposed to a concentration above this value can experience irritation of the eyes, nose, and respiratory system, while higher concentrations (250 ppm) can cause death.^{8,11} Nowadays, commercially available H₂S detectors rely on either electrochemical or solid-state metal oxide sensors. While the former are difficult to miniaturize and rather expensive, the latter suffer from poor selectivity and heavy

humidity cross-sensitivity. Additionally, both types of sensors allow for reliably estimating H₂S concentrations in the tens of parts per million range with uncertainties near ± 5 ppm. Therefore, there is a need and a strong industry-driven demand for developing a new generation of reliable, robust, accurate, and cost-effective sensors with enhanced sensitivity and selectivity, reduced moisture cross-sensitivity, and response time to facilitate the early detection of H₂S in the environment, before its concentration reaches potentially hazardous levels.

In the past few years, n-type metal oxide semiconductors (i.e., SnO₂, In₂O₃, ZnO, or WO₃) with different morphologies such as nanoparticle films or one-dimensional (1D) nanostruc-

Received: January 14, 2015

Accepted: March 16, 2015

Published: March 16, 2015

tures, have been intensively explored as potential building blocks for H_2S gas sensors.^{12–17} Research on 1D single-crystalline metal oxide nanostructures including nanowires, nanotubes, nanoneedles, nanorods, and nanobelts has been favored in recent years because their ultrahigh surface-to-volume ratio, low number of defects, and good stability within a wide range of operating temperatures make them an excellent building block for micro/nanoscale gas sensors.^{18–21} Yet, the lack of selectivity and humidity cross-sensitivity still remain the major drawbacks to overcome. Many works have shown that, by adding catalyst nanoparticles onto the metal oxide matrix (i.e., surface functionalization of the low-dimensional metal oxide), the selectivity toward a target gas can be significantly increased.^{21–26} In general, the growth of functionalized, nanostructured materials employs a multistep approach in which in the first step the nanostructured materials are synthesized. This is followed in the second step by a functionalization in which metal nanoparticles are deposited onto the surface of the previously grown nanostructures. In some cases, the process still needs a third step in which the as-deposited metal nanoparticles are oxidized. This involved, multistep process cannot be easily scaled up and, therefore, will hardly be adopted by the industry for mass production of sensors.^{27,28} The use of n-type metal oxide nanomaterials functionalized with p-type cupric oxide (CuO) nanoparticles has been reported to be advantageous for detecting H_2S . Shao and co-workers reported on CuO nanoparticle decorated SnO_2 nanowires for detecting H_2S with high sensitivity and remarkable selectivity.²⁹ Yet, the response time of their sensor was rather long (i.e., 3 min), and the response was significantly reduced for H_2S concentrations below 1 ppm. Furthermore, the sensing material was produced following a time-consuming three-step technique that included two conventional chemical vapor deposition (CVD) processes followed by a 24 h oxidation (for growing the metal oxide nanowires, decorating them with copper nanoparticles, and oxidizing the latter to CuO). Sun and co-workers also addressed the detection of H_2S using CuO/SnO_2 nanowires.³⁰ Although their sensor was not as responsive as the one presented by Shao and co-workers, the response time was clearly improved down to 9 s. However, the synthesis process remained complex and lengthy. Wu and co-workers studied ZnO nanorods for the detection of H_2S at room temperature.³¹ Although a remarkable response was obtained for 1 ppm of H_2S , a rather long response time of about 20 min was observed, and the sensor was unable to recover its original baseline after exposure to the analyte. Finally, none of the papers cited above reported the effect of the ambient humidity on the sensor response, yet it is well-known that humidity cross-sensitivity is a major problem experienced with metal oxide gas sensors.

Recently, we have shown that aerosol-assisted chemical vapor deposition (AACVD) is a suitable method for growing, in a single step, WO_3 nanoneedles decorated with metal nanoparticles.^{20,24,25,32} Unlike in conventional CVD, where precursors must be volatile and thermally stable, AACVD allows for the use of a wide range of precursors owing to its solution-delivery-based principle.¹² Furthermore, the AACVD process is conducted at lower temperatures than CVD, typically in a range between 350 and 600 °C, which makes it suitable for the direct, bottom-up integration of gas-sensitive nanomaterials onto a wide spectrum of substrates including glass, ceramic, silicon micro/electromechanical systems (MEMSs), or even flexible polymeric.³³ In this paper, we report, for the first time,

on the direct growth of WO_3 nanoneedles decorated with p-type Cu_2O nanoparticles onto MEMS hot plates in a single step by using AACVD. To the best of our knowledge, CVD routes have not been used before to grow WO_3 nanoneedles and simultaneously decorate them with nanoparticles of copper oxides, all in a single step and avoiding a further oxidation step. This new route is, therefore, advantageous in terms of the time needed to grow these hybrid nanomaterials. Scanning electron microscopy (SEM), X-ray diffraction (XRD), transmission electron microscopy (TEM), high-resolution TEM (HRTEM), X-ray photoelectron spectroscopy (XPS), and near-edge X-ray absorption fine-structure transmission X-ray microscopy (NEXAFS-TXM) have been employed to determine the phase composition, morphology, and microstructure of the as-nanoneedle mats. Their gas-sensing properties toward H_2S in both dry and humid backgrounds have been studied, together with their response to other gases or vapors. Finally, in light of the experimental findings, a sensing mechanism for H_2S in Cu_2O -decorated WO_3 nanoneedles is introduced and discussed.

RESULTS AND DISCUSSION

Materials Characterization. Pure WO_3 nanoneedles were obtained from AACVD of $\text{W}(\text{CO})_6$ at 500 °C. WO_3 nanoneedles decorated with Cu_2O were grown in a single step at a lower temperature of 380 °C from AACVD of a mixture of $\text{W}(\text{CO})_6$ and $\text{Cu}(\text{acac})_2$. The as-deposited films (WO_3 and $\text{Cu}_2\text{O}/\text{WO}_3$) were strongly adherent to the substrate, with dark blue and dark maroon-blue color, respectively. After annealing at 500 °C for 3 h, the color of both samples changed and became white-yellow. The morphology of the synthesized materials was characterized by SEM. Figure 1 depicts the SEM images obtained from the as-deposited layers. The results confirm the formation of a thicker layer of nonaligned nanoneedle-like structures, with high density and homogeneous distribution over the substrate. The nanoneedles of pure WO_3 (Figure 1a,c) were $\sim 11\ \mu\text{m}$ long, and their diameters varied between 50 and 100 nm.

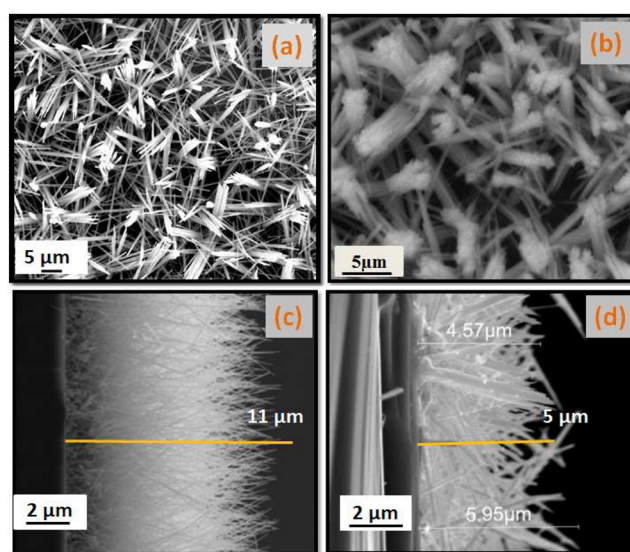


Figure 1. SEM images of the as-deposited (a) pure WO_3 nanoneedles, (b) Cu_2O -functionalized WO_3 nanoneedles, (c) cross section of pure WO_3 nanoneedles, and (d) cross section of Cu_2O -functionalized WO_3 nanoneedles.

Cu₂O/WO₃ nanoneedles (Figure 1b,d) were 5 μ m long with a thicker diameter that ranged between 50 and 240 nm; agglomerates of two, three, or more nanoneedles are also visible. This difference in the morphology of the nanoneedles grown in functionalized and nonfunctionalized samples could be attributed to the growth temperature and/or solvent used.³⁴

XRD analysis (Figure 2) of the different samples indicated formation of the monoclinic phase WO₃ nanoneedles [*P21/n*

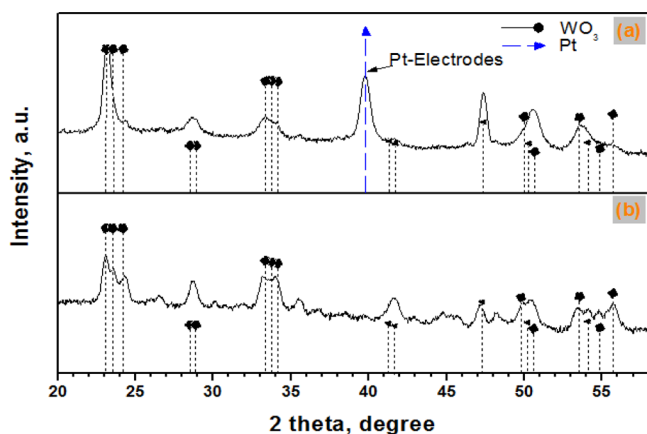


Figure 2. XRD patterns of (a) pure WO₃ nanoneedles and (b) Cu₂O-functionalized WO₃ nanoneedles.

(No. 14) space group, with typical cell parameters of $a = 0.729$ nm, $b = 0.7539$ nm, $c = 0.7688$ nm, and $\beta = 90.91^\circ$; ICDD card no. 72-0677]. From the pure WO₃ pattern, it is clear that the nanoneedles were strongly oriented in the (002) direction, showing an intense diffraction peak at $2\theta = 23.10^\circ$. Furthermore, a strong platinum reflection at $2\theta = 39.9^\circ$ was observed coming from the electrodes. For the pattern recorded from the functionalized sample, the nanoneedles were

randomly oriented, with the absence of any reflections from copper oxides.

Elemental and chemical characterizations of the films were performed by XPS. In this work, we do not show the XPS and HRTEM results obtained from the pure WO₃ film because they were similar to the ones reported in our previous works.^{20,35} Figure 3a shows the W 4f XPS spectrum recorded on a Cu₂O/WO₃ sample and its fitting analysis. To reproduce the spectrum, two doublets, a singlet, and the Shirley background were employed. The component centered at 38.6 eV is due to photoelectrons emitted from the W 5p_{3/2} core level. The highest-intensity doublet peak (W 4f_{7/2}), centered at 35.5 eV, is generated by photoelectrons emitted from W atoms with the oxidation state 6+, i.e., stoichiometric WO₃.³⁶ Therefore, the W ions have their 5d shell empty; i.e., there are no cation d electrons available to be transferred to the adsorbates. The second W 4f doublet, found at 2 eV lower binding energy, is generated by photoelectrons emitted from W atoms with the oxidation state 4+.³⁷ In this case, the d-electron orbitals on adjacent cations are partially occupied. These reduced cations provide active sites for chemisorption and catalytic activity, i.e., determine the gas-sensing activity of the films.³⁸ From the area ratio of the components used to fit the W 4f peak, we evaluated that near 35% of the W atoms have the oxidation state 4+, thus contributing to gas detection. This result is supported by analysis of the O 1s XPS spectrum, which is reproduced by two singlets (Figure 3b). The first component is centered at 530.5 eV, and it is assigned to the O atoms that form the strong W_{1/4}–O bonds in the oxide.³⁹ The second component at about 531.7 eV (37% of the total O 1s area) has been attributed to O atoms in substoichiometric WO_x structures.⁴⁰

Figure 3c shows the Cu 2p core-level spectrum, which consists of two sets of peaks: a low-intensity doublet at 942.6 and 962.8 eV, which corresponds to CuO, and a more intense

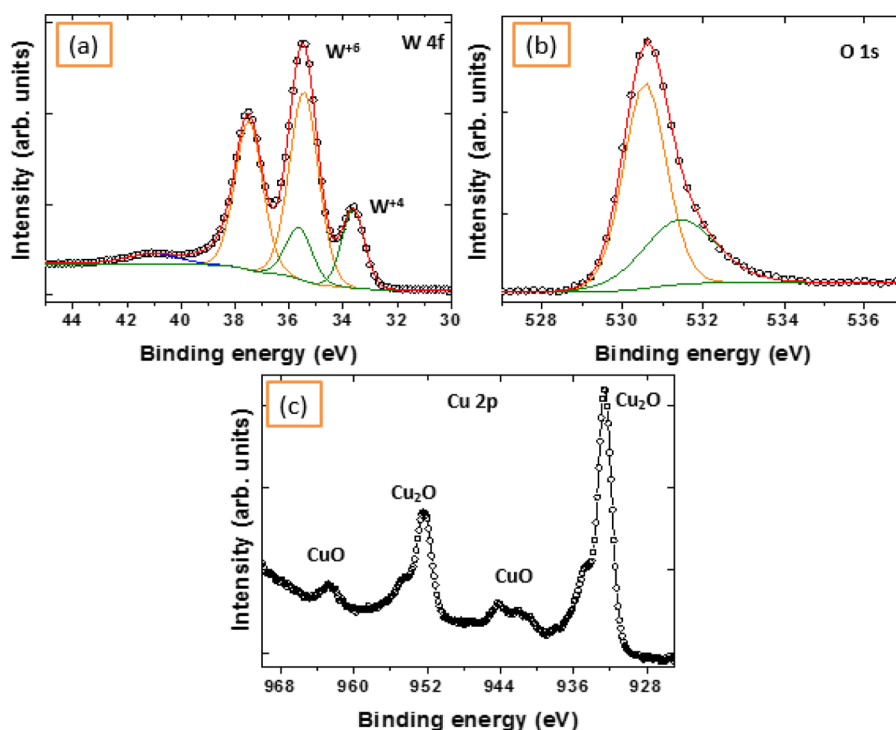


Figure 3. Typical XPS spectra of the Cu₂O-nanoparticle-decorated WO₃ nanoneedles: (a) W 4f; (b) O 1s; (c) Cu 2p.

doublet whose components are centered at 932.6 and 952.3 eV, which corresponds to either copper metal or Cu_2O .

In order to experimentally clarify to which oxidation state this doublet belongs, we have analyzed our sample by NEXAFS-TXM. NEXAFS probing the density of states of partially filled or completely unfilled electronic states is very sensitive to the local bonding environment, particularly to the number of valence electrons, symmetry, and coordination number of the material structural unit cell.⁴¹ Figure 4 illustrates

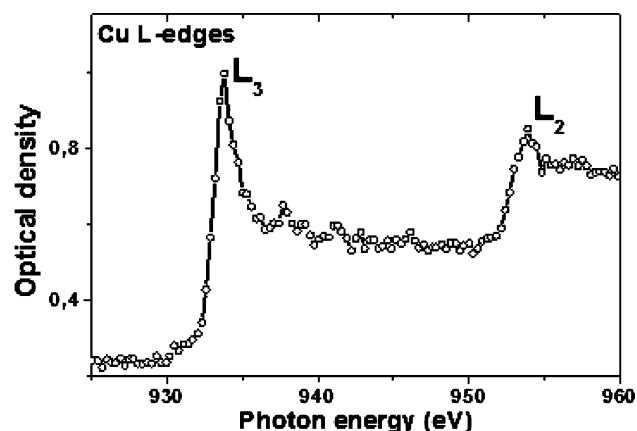


Figure 4. NEXAFS-TXM spectrum of Cu L-edges of nanoparticle-decorated WO_3 nanoneedles. The energy separation between L_3 and L_2 is 21.0 eV, which is characteristic for Cu_2O .

the Cu L-edge NEXAFS spectrum, which is characterized by a low-intensity feature at ~ 930.8 eV attributed to CuO and two relative intense features at ~ 932.8 and ~ 953.5 eV. These two intense features that arise from the dipole transitions of the Cu $2p_{3/2}$ and Cu $2p_{1/2}$ core levels into the empty d states are associated with the presence of Cu_2O , as reported in ref 42. Therefore, XPS and NEXAFS analysis together testify for the presence of CuO and Cu_2O in the sample, with 88% of the Cu atoms in the Cu_2O form and 12% in the CuO form.

Details of the morphological and structural features of Cu_2O -decorated WO_3 nanoneedle mats were studied by TEM and HRTEM. Parts a and b of Figure 5 display low-magnification TEM images of $\text{Cu}_2\text{O}/\text{CuO}$ nanoparticles decorating the nanoneedles. The formation of nanoparticles with average diameter of about 2–3 nm and the existence of a few bigger ones with diameter of about 7 nm can be observed. In addition, a thin amorphous layer surrounding the nanoneedles can also be seen, the formation of which can be associated with combustion of the solvents during the AACVD process. Analysis of the HRTEM images (Figure 5c,d) reveals the coexistence of Cu_2O and CuO crystallites in the $\text{Cu}_2\text{O}/\text{WO}_3$ nanoneedle mats.

As derived from TEM images, the fringe patterns with interspacing distances of 0.218, 0.244, and 0.212 nm are similar to the interplanar distances of the (200), (111), and (200) lattice planes of Cu_2O , respectively (ICDD-PDF card no. 00-005-0667), whereas that with an interspacing distance of 0.177 nm is in good agreement with the interplanar distance of the (112) lattice planes in bulk crystalline CuO (ICDD-PDF card no. 00-045-0937). Hence, these results suggest that the smaller nanoparticles, which represent the vast majority, correspond to Cu_2O and the larger ones correspond to CuO . In summary, XPS, NEXAFS-TXM, and HRTEM results imply that both

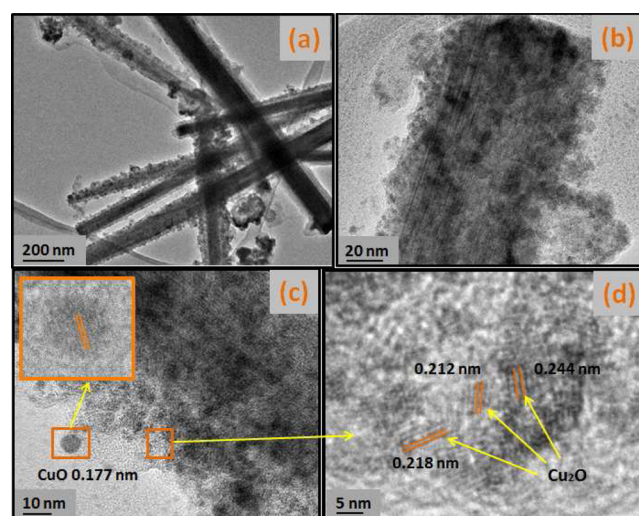


Figure 5. TEM and HRTEM images of the obtained Cu_2O -functionalized WO_3 nanoneedles: (a and b) low magnification; (c and d) high magnification.

CuO and Cu_2O coexist in the samples, with Cu_2O being more profuse.

Gas-Sensing Response. The gas-sensing properties toward 5 ppm of H_2S of pristine WO_3 and Cu_2O -functionalized WO_3 nanoneedles were examined at operating temperatures ranging from 270 to 390 $^\circ\text{C}$. This concentration is 2 times lower than the maximum permissible exposure limit to H_2S .^{8–10} The maximum operating temperature was selected to ensure the safe operation of the sensor transducer (i.e., avoiding membrane damages or drift in the heating element). The results are shown in Figure 6.

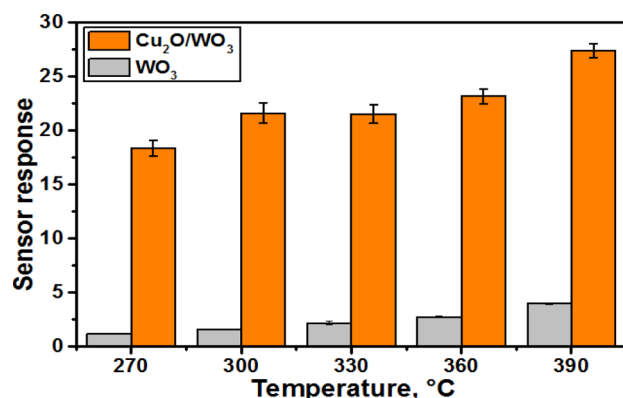


Figure 6. Sensor responses and error bars to 5 ppm of H_2S as a function of the operating temperature.

$\text{Cu}_2\text{O}/\text{WO}_3$ samples showed stable and very high responses all over the operating temperatures tested. In contrast, pure WO_3 nanoneedles displayed good and stable responses at temperatures equal to or exceeding 280 $^\circ\text{C}$, while below this value, they exhibited unsaturated responses, with drift in the baseline resistance. For the range of temperatures tested, the sensor response increases when the operating temperature is increased. Generally, in metal oxides, the optimal working temperature depends on the quantity of the adsorbed oxygen ionic species and the energy needed to enable reactions between these ionic species and a target gas.^{43,44} The highest response recorded from pristine WO_3 samples toward 5 ppm of

H₂S was 4, while it reached 27.5 for Cu₂O/WO₃ nanoneedles. Thus, the decoration with Cu₂O nanoparticles of WO₃ nanoneedles has resulted in a 7-fold increase in the sensor response.

In subsequent studies, 390 °C was chosen as the optimal working temperature of the sensors.

Figure 7 depicts the responses obtained from the sensors to various concentrations of H₂S at the optimal working

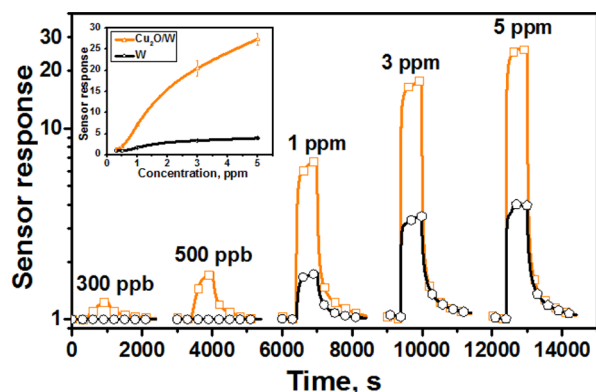


Figure 7. Sensor response to various concentrations of H₂S at 390 °C. The inset shows the curves of response versus concentration.

temperature. The insets show the curves of the response versus concentration. From these results, it is evident that the gas sensor response increases when the concentration of the analyte is increased. Furthermore, at parts per billion levels (100 and 500 ppb), pristine WO₃ was not able to detect H₂S, whereas by the addition of Cu₂O, the detection limit has been improved and is now below 300 ppb.

Figure 8 shows an example of the responses recorded from pristine WO₃ and Cu₂O/WO₃ sensors toward 1 ppm of H₂S at 390 °C. Overall, the sensors behave as n-type semiconductors, i.e., decreasing the resistance when exposed to a reducing gas (H₂S). The sensors displayed stable and reproducible responses, and no drift in the response was observed. It is

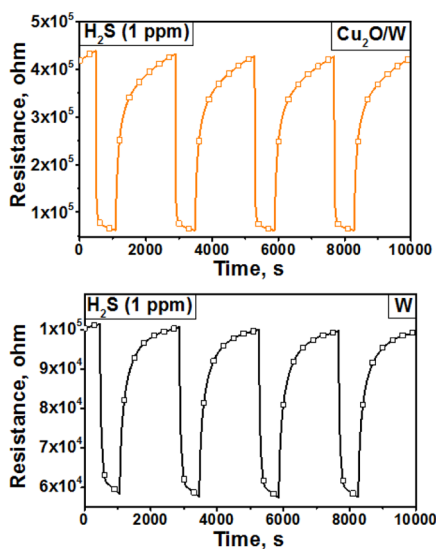


Figure 8. Example of the responses recorded from pristine WO₃ (bottom) and Cu₂O/WO₃ (top) sensors toward 1 ppm of H₂S at 390 °C.

well-known that the quality of the semiconductor-based gas sensor material affects the stability of the sensor, and thus the high crystallinity of our WO₃ nanoneedles is responsible for the high stability of the sensors.

In addition, we can see from the response curves that decorating the WO₃ nanoneedles with Cu₂O nanoparticles results in the baseline resistance of the sensor being increased. Cu₂O is a well-known p-type semiconductor, and WO₃ is an n-type one; thus, p–n junctions are formed at the interfaces of the Cu₂O/WO₃ nanocomposite. The formation of these leads to the appearance of a space charge layer around each Cu₂O/WO₃ interface, which decreases the free electrons in the conduction band of WO₃ nanoneedles and, therefore, increases the baseline resistance of the sensor.⁴⁵ At 5 ppm of H₂S, the response and recovery times were calculated for pristine and decorated WO₃ nanoneedles (Figure 9). The results indicate

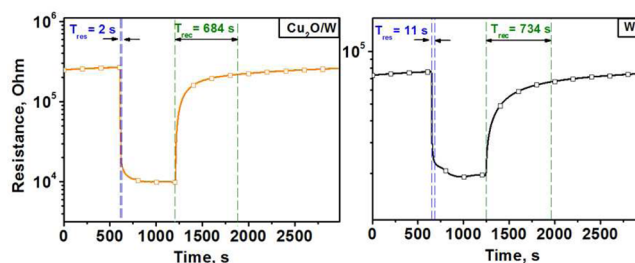


Figure 9. Enlarged responses of functionalized and nonfunctionalized WO₃ sensors to 5 ppm of H₂S at 390 °C. The response time, T_{res} , and recovery time, T_{rec} , correspond to a 90% change in the electrical resistance of the samples.

that Cu₂O-decorated samples responded nearly 6 times faster (i.e., 2 s) than nonfunctionalized samples (i.e., 11 s). When this result is compared with the ones reported in the literature for metal/metal oxide nanoparticle-functionalized metal oxide nanowire nanocomposite films, it can be concluded that such a fast response time has not been reported until now. A complete recovery of the baseline resistance was observed within 1100 s after the removal of H₂S for both pristine and decorated samples.

The selectivity of the sensors toward H₂S was studied by measuring the response to different interfering gases such as H₂ (500 ppm), CO (50 ppm), NH₃ (50 ppm), C₆H₆ (30 ppm), and NO₂ (40 ppb). All of these concentrations are much higher than those one could expect to find in ambient air.⁴⁶ As shown in Figure 10, it is clear that Cu₂O-decorated WO₃ nanoneedle sensors are more sensitive to low concentrations of H₂S (5 ppm) than to high concentrations of the interfering gases.

The response of the Cu₂O/WO₃ sensor to H₂S is almost 7 times higher than that to H₂ and C₆H₆, 13 times higher than that to CO, and 9 times higher than that to NH₃ vapors. It is worth noting that Cu₂O-decorated WO₃ nanoneedles show significant cross-sensitivity to NO₂, as opposed to pure WO₃ nanoneedles, which show an ultrahigh sensitivity toward trace concentrations of NO₂ (i.e., more than 100 times higher than that to the other species studied). Therefore, the combination of two sensors, namely, a Cu₂O-decorated and a pristine WO₃ nanoneedle sensor in a H₂S detector, would enable suppression of the NO₂ cross-sensitivity.

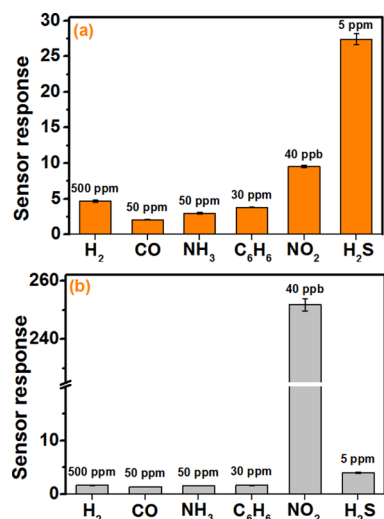


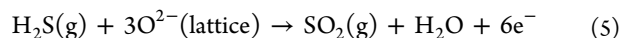
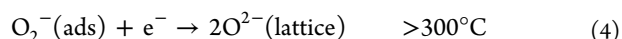
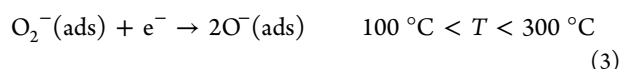
Figure 10. Selectivity diagram of (a) functionalized and (b) nonfunctionalized WO₃ gas sensors toward different gases at 390 °C.

■ GAS-SENSING MECHANISM

It has been shown that Cu₂O-decorated WO₃ nanoneedles exhibit a remarkably improved H₂S response compared to pristine WO₃ nanoneedles. To explain the sensing mechanism for H₂S, the surface adsorption and reaction model illustrated in Figure 11 is suggested. When pristine WO₃ nanoneedles are exposed to air, oxygen molecules can adsorb on their surface and form chemisorbed oxygen species such as O₂⁻, O⁻, or O²⁻. The nature of oxygen adsorbates depends on the operating temperature (eqs 1–4), and above 300 °C, the predominant oxygen ions adsorbed are O²⁻(lattice).⁴³ Oxygen adsorbates lead to the formation of an electron-depletion layer because they trap electrons from the conduction band of the n-type WO₃ nanoneedles, which makes the material highly resistive.

When the sensor is exposed to H₂S, the chemisorbed oxygen species [O²⁻(lattice)] can react with the reducing gas

molecules, giving H₂O(g) and SO₂(g) following eq 5,^{29,47} while the electrons, originally trapped as oxygen adsorbates, will be released, which eventually results in a decrease in the resistance of the nanoneedle mats (Figure 11a).



In contrast, Cu₂O/CuO-decorated WO₃ nanoneedles show a different mechanism (Figure 11b,c). Cu₂O/CuO nanoparticles and WO₃ nanoneedles are p- and n-type semiconductor oxides, respectively. The contact between these two different materials leads to the formation of numerous p–n heterojunctions and electron-depletion layers at the interface between WO₃ nanoneedles and Cu₂O/CuO nanoparticles. Upon exposure to H₂S, three simultaneous reactions can take place:

One corresponds to the interaction between the studied gas and chemisorbed oxygen, which is described above eq 5. The two others correspond to the interaction between H₂S molecules and Cu₂O/CuO nanoparticles. According to eqs 6 and 7, Cu₂O and CuO are converted to metallic Cu₂S and CuS, respectively, by an oxygen/sulfur replacement mechanism,⁴⁸ while the p–n heterojunctions are destroyed. Hence, a large number of electrons are released in the WO₃ nanoneedles, and a dramatic decrease in the resistance of the nanocomposite mat can be measured. Evidence on the formation of metallic Cu₂S and CuS compounds has been shown by the XPS spectra recorded from the active layer after H₂S measurement (Figure S1 in the Supporting Information, SI).

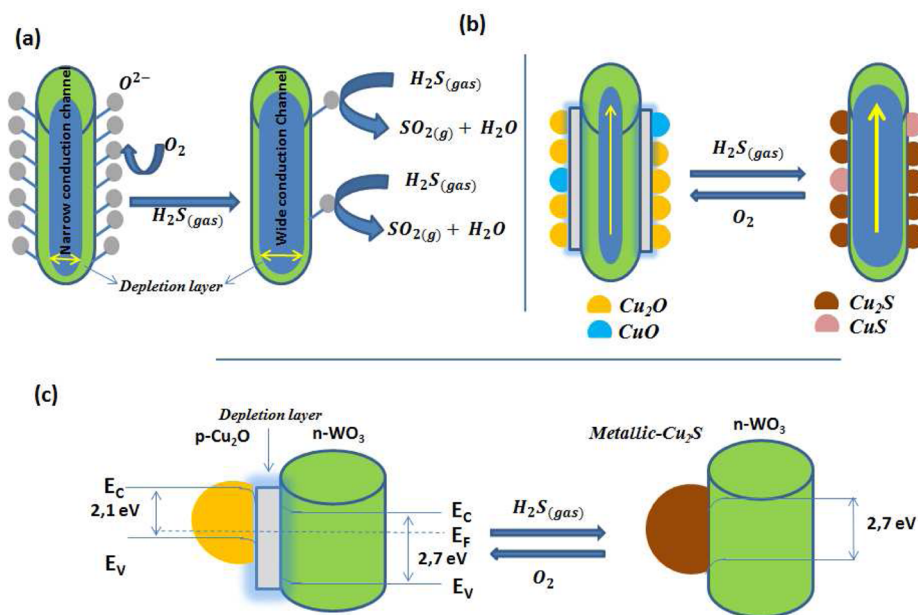
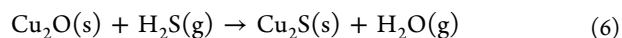
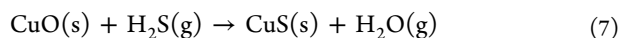
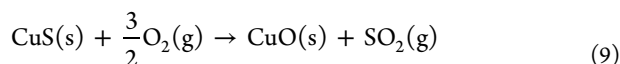
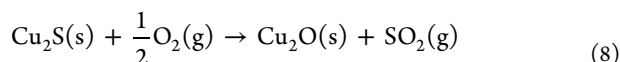


Figure 11. H₂S gas-sensing mechanism of (a) pure WO₃ nanoneedles and (b) Cu₂O/CuO-functionalized WO₃ nanoneedles and an example of the p–n heterojunction of the Cu₂O nanoparticles/WO₃ nanoneedles before and after H₂S analyte (c).



In the recovery phase, where synthetic air is flushed to clean the sensor surface, the copper oxides are regenerated according to eqs 8 and 9, the p–n heterojunctions are restored, and the material resistance returns to its original high value.



Humidity Cross-Sensitivity. The influence of water vapor is a key factor to be taken into consideration for the development of chemoresistive metal oxide gas sensors. Ambient moisture can produce notable changes in the electrical properties of metal oxides and dramatically influences the sensitivity.

To study the effect of humidity, the response of the sensors toward 5 ppm of H_2S at an operating temperature of 390 °C was monitored under both dry and humid [50% relative humidity (RH) at 25 °C] conditions. Figure 12 shows two consecutive cycles of response to H_2S and recovery in air under humid and dry conditions.

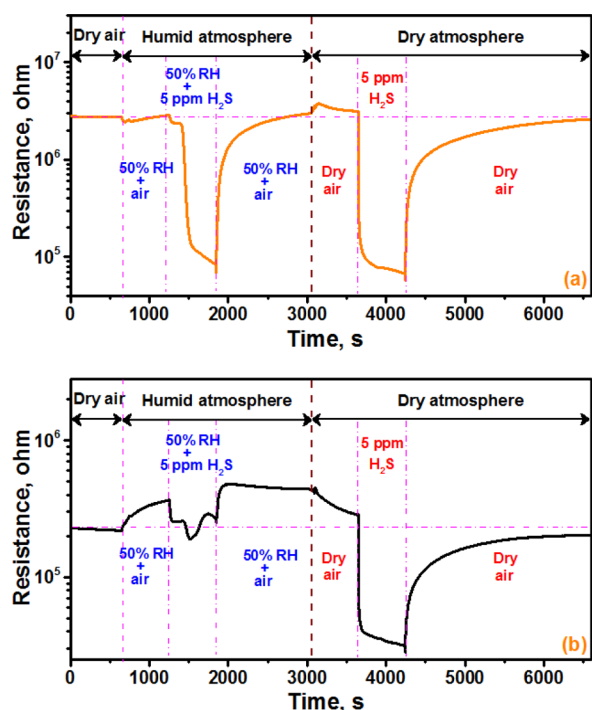


Figure 12. Sensor resistance variation of (a) functionalized and (b) nonfunctionalized WO_3 nanoneedles toward dry and humid (50% RH at 25 °C) atmospheres in a background of synthetic air and 5 ppm of H_2S in synthetic air.

From these results, it can be derived that there is a high influence of ambient moisture on the response of pristine WO_3 nanoneedles. When humid air is introduced in the background, the resistance of the pristine WO_3 sensor is increased by 40% compared to its baseline resistance in dry air. This increase in the resistance under humid conditions has been reported before for SnO_2 , ZnO , and In_2O_3 .^{49–52} Under humid conditions, the response of pristine WO_3 nanoneedles to H_2S is dramatically reduced by 82%, which indicates the occurrence of a

competition between water molecules (formation of hydroxyl groups) and H_2S for active sites. It is well-known that there is a high dependence between the effect of the humidity on the sensor response and the relative surface distribution of hydroxyl groups and oxygen species.^{49–52} When humidity is removed, the baseline resistance is restored and so is the sensor response to H_2S .

For Cu_2O -decorated WO_3 nanoneedles, small changes in the baseline resistance (below 5%) and response to H_2S (below 15%) can be observed when the sensor is operated under humid or dry conditions. The fact that the sensor baseline and the response mechanism to H_2S are dominated by the p–n heterojunctions brought in by the presence of Cu_2O nanoparticles rather than by surface oxygen species explains the high immunity of this nanomaterial to dramatic changes in the background humidity. A summary of the sensing properties of the $\text{Cu}_2\text{O}/\text{WO}_3$ nanomaterial and a comparison with those reported by previously published works can be found in Table S1 in the SI.

CONCLUSIONS

Because of its simplicity, relatively low setup and running costs, and scalability, AACVD is an industrially attractive technique. Because it is an atmospheric pressure process, the rates of deposition are typically orders of magnitude higher than those of low-pressure processes, which allows for the direct and fast growth of nanomaterials onto a wide spectrum of substrates. WO_3 nanoneedles decorated with Cu_2O nanoparticles were successfully grown onto MEMS gas-sensor substrates via a single-step AACVD. This route compares very favorably in terms of the time needed for growing these nanomaterials to previously reported methods (i.e., 30 min vs nearly 24 h). The gas-sensing results have revealed that the decoration of WO_3 nanoneedles with Cu_2O nanoparticles dramatically increases their response to H_2S (i.e., a 700% increase in comparison to that of pristine WO_3 nanoneedles). A low detection limit below 300 ppb has been demonstrated. Furthermore, this hybrid nanomaterial shows the fastest response time ever reported (2 s) and very low moisture cross-sensitivity, which is rarely found in metal oxides. Consequently, these results pave the way for a new generation of nanotechnology-enabled H_2S analyzers with superior performance.

EXPERIMENTAL SECTION

Functionalized and nonfunctionalized WO_3 nanoneedles were directly deposited on MEMS microhot plates using the AACVD method. Figure 13 depicts four microsensor platforms; each one contains POCl_3 -doped polysilicon double-spiral-shape heaters (16 Ω/sq , 0.47 μm thickness, and $\text{TCR} = 6.79 \times 10^{-4}/^\circ\text{C}$) and platinum electrodes (0.2 μm thickness, electrode gap = 50 μm). To electrically insulate the electrodes on top from the heater, 800-nm-thick silicon oxide layers were produced at the wafer level following various microfabrication steps including implantation, photolithography, metallization, lift-off, and rear side etching of the substrate to define the membranes. The synthesis of pristine WO_3 nanoneedles was carried out via AACVD of tungsten hexacarbonyl [50 mg, $\text{W}(\text{CO})_6$, Sigma-Aldrich, $\geq 97\%$] dissolved in a mixture of acetone and methanol (15 mL of acetone and 5 mL of methanol, Sigma-Aldrich, $\geq 99.6\%$), whereas the Cu_2O -functionalized WO_3 nanoneedles were obtained by mixing tungsten hexacarbonyl [50 mg, $\text{W}(\text{CO})_6$, Sigma-Aldrich, $\geq 97\%$] dissolved in methanol (16 mL of methanol, Sigma-Aldrich, $\geq 99.6\%$) with copper(II) acetylacetonate [7 mg, $\text{Cu}(\text{acac})_2$, Sigma-Aldrich, 99.9%] dissolved in chloroform (4 mL of chloroform, Sigma-Aldrich). The arrays of four membranes were cleaned with acetone and then with ethanol, dried in air, and then placed inside the reactor. A micromask

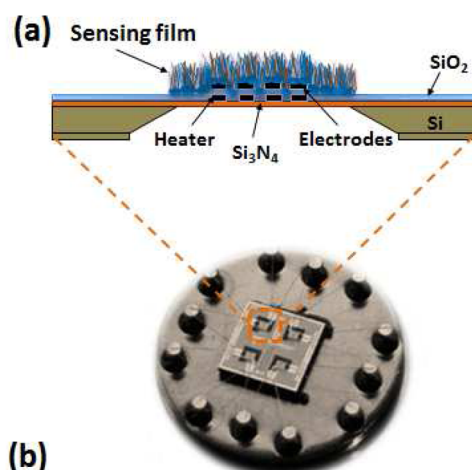


Figure 13. Schematic view of the gas-sensor section (a) and a photo image of the micromachined sensor mounted on a standard TO-8 package (b).

was placed on the top of the substrate to cover the electrical connections of the heater and electrodes. The solutions were kept in a glass flask and placed in an ultrasonic humidifier. The aerosol of solvents and the mixture of precursors were transported to the heated zone inside the reactor by using 500 mL/min of nitrogen as a carrier gas. The exhaust from the reactor was vented directly into the extraction system of a fume cupboard. The deposition time was between 30 and 45 min, until all of the precursor had passed through the reactor. After that, all of the samples were subjected to annealing at 500 °C for 3 h under a constant flow (200 sccm) of synthetic air (Praxair, 99.99%). Finally, the microsensors were wire-bonded to standard TO-8 packages.

The surface morphology of the samples was investigated using a scanning electron microscope (FEI Quanta 600) and transmission electron microscopes (Jeol JEM 1011, operating at 100 kV, and Jeol 2100, operating at 200 kV), while the structure of the deposited film was studied by XRD (Bruker, AXD D8-Discover, using Cu K α radiation operated at 40 kV and 40 mA). The elemental and chemical composition determinations were performed by XPS (Physical Electronics, VERSAPROBE PHI 5000, using monochromatic Al K α radiation with 0.7 eV energy resolution, a dual-beam charge neutralizer composed of an electron gun (\approx 1 eV), and an argon-ion gun (\leq 10 eV) for charge compensation; all of the binding energies were calibrated to the C 1s peak at 284.5 eV).

To study the electronic structure of a single wire, NEXAFS-TXM was performed with the full-field transmission X-ray microscope installed at the undulator beamline U41-SGM at the electron storage ring BESSY II operated by the Helmholtz-Zentrum Berlin.^{53–57} The spectra were recorded at room temperature in a transmission mode by taking a sequence of images over a range of photon energies covering the investigated absorption edges with a spectral resolution larger than 5000. The used zone plate allowed a spatial resolution of 25 nm. The NEXAFS spectra were normalized because the photon flux varies as a function of the photon energy ($h\nu$) and the position in the object field (x, y). The normalization was performed by dividing the function $I(x, y, h\nu)$ recorded on the sample by the photon flux curve $I_0(x+dx, y+dy, h\nu)$ recorded in its sample free proximity at position $(x+dx, y+dy)$. Both $I(x, y, h\nu)$ and $I_0(x, y, h\nu)$ were recorded in the same image stack because, near each studied nanostructure, bare regions permit the measurement of I_0 .

Gas-sensing tests of the sensors were carried out in a Teflon/stainless steel test chamber (2×10^{-2} dm³) under a continuous gas flow of 200 sccm. The resistance change of the different samples, while exposed to different concentrations of the studied gases and vapors, was monitored by using an Agilent-34970A multimeter. The desired concentrations of the test gases were obtained by employing calibrated gas bottles and PC-driven mass flow controllers (Bronkhost Hitech

7.03.241). Humidity measurements were performed using an Environics series 4000, which allowed us to automatically mix up to three individual gases in a balance gas (air, pollutant gas, and humidity). The sensors were exposed to the test gas for 10 min, and subsequently the chamber was purged with air for 30 min, which enabled recording recovery of their baseline resistance. After this process, the sensors were ready for a new measurement. The sensor response (R) was defined as $R = R_a/R_g$ for reducing gases and $R = R_g/R_a$ for oxidizing gases, where R_a and R_g are the sensor resistances at the stationary state in air and after 10 min of exposure to analytes, respectively. Moreover, the response time is defined as the time needed by the sensor to reach a fixed percentage (e.g., 110%) of its steady-state resistance value when it is exposed to a reducing gas (H₂S), whereas the recovery time is outlined as the time needed by the sensor to return to a fixed percentage (e.g., 90%) of the saturation value of its resistance when it is subjected to clean air.

■ ASSOCIATED CONTENT

■ Supporting Information

Summary of the sensing properties of the Cu₂O/WO₃ nanomaterial, comparison with previously published works, and XPS spectra recorded from the Cu₂O/WO₃ active layer after the H₂S measurements. This material is available free of charge via the Internet at <http://pubs.acs.org>.

■ AUTHOR INFORMATION

Corresponding Author

*E-mail: eduard.llobet@urv.cat.

Notes

The authors declare no competing financial interest.

■ ACKNOWLEDGMENTS

This work has been supported, in part, by the Spanish Ministry of Science and Innovation via Grant TEC2012-32420 and also by the Catalan Institution for Research and Advanced Studies via the ICREA Academia Award (to E.L.). We thank the Helmholtz-Zentrum Berlin for allocation of synchrotron radiation beamtime. The research leading to these results has received funding from the European Community's Seventh Framework Programme (FP7/2007-2013) under Grant Agreements 226716 (ELISA) and 312284 (CALIPSO). C.B. is a Research Associate of the National Funds for Scientific Research (FRS-FNRS, Belgium). S.V. is supported by the SoMoPro II Programme, co-financed by the European Union and the South-Moravian Region, via Grant 4SGA8678.

■ REFERENCES

- (1) Vallejos, S.; Stoycheva, T.; Annanouch, F. E.; Llobet, E.; Umek, P.; Figueras, E.; Cané, C.; Gracia, I.; Blackman, C. Microsensors Based on Pt–Nanoparticle Functionalised Tungsten Oxide Nanoneedles for Monitoring Hydrogen Sulfide. *RSC Adv.* **2014**, *4*, 1489–1495.
- (2) Ghosh, S.; Roy Chaudhuri, C.; Bhattacharya, R.; Saha, H.; Mukherjee, N. Palladium–Silver-Activated ZnO Surface: Highly Selective Methane Sensor at Reasonably Low Operating Temperature. *ACS Appl. Mater. Interfaces* **2014**, *6*, 3879–3887.
- (3) Zhang, S.; Zhang, P.; Wang, Y.; Ma, Y.; Zhong, J.; Sun, X. Facile Fabrication of a Well-Ordered Porous Cu-Doped SnO₂ Thin Film for H₂S Sensing. *ACS Appl. Mater. Interfaces* **2014**, *6*, 14975–14980.
- (4) He, L.; Jia, Y.; Meng, F.; Li, M.; Liu, J. Development of Sensors Based on CuO-Doped SnO₂ Hollow Spheres for ppb Level H₂S Gas Sensing. *J. Mater. Sci.* **2009**, *44*, 4326–4333.
- (5) North Carolina Department of Environment and Natural Resources. Summary of Rule Amending the Hydrogen Sulfide Acceptable Ambient Level, <http://daq.state.nc.us/toxics/studies/H2S/> (accessed Mar 15, 2006).

- (6) Wagh, M. S.; Patil, L. A.; Seth, T.; Amalnerkar, D. P. Surface Cupricated SnO_2 – ZnO Thick Films as a H_2S Gas Sensor. *Mater. Chem. Phys.* **2004**, *84*, 228–233.
- (7) Meng, F.; Di, X.; Dong, H.; Zhang, Y.; Zhu, C.; Li, C.; Chen, Y. Ppb H_2S Gas Sensing Characteristics of $\text{Cu}_2\text{O}/\text{CuO}$ Sub-Microspheres at Low-temperature. *Sens. Actuators, B* **2013**, *182*, 197–204.
- (8) Qi, G.; Zhang, L.; Yuan, Z. Improved H_2S Gas Sensing Properties of ZnO Nanorods Decorated by a Several nm ZnS Thin Layer. *Phys. Chem. Chem. Phys.* **2014**, *16*, 13434–13439.
- (9) Ghimbeu, C. M.; Lumberras, M.; Siadat, M.; Landschoot, R. C.; Schoonman, J. Electrostatic Sprayed SnO_2 and Cu-Doped SnO_2 Films for H_2S Detection. *Sens. Actuators, B* **2008**, *133*, 694–698.
- (10) Kaur, M.; Jain, N.; Sharma, K.; Bhattacharya, S.; Roy, M.; Tyagi, A. K.; Gupta, S. K.; Yakhmi, J. V. Room-Temperature H_2S Gas Sensing at ppb Level by Single Crystal In_2O_3 Whiskers. *Sens. Actuators, B* **2008**, *133*, 456–461.
- (11) Samokhvalov, A.; Tatarchuk, B. J. Characterization of Active Sites, Determination of Mechanisms of H_2S , COS and CS_2 Sorption and Regeneration of ZnO Low-Temperature Sorbents: Past, Current and Perspectives. *Phys. Chem. Chem. Phys.* **2011**, *13*, 3197–3209.
- (12) Stoycheva, T.; Annanouch, F. E.; Gràcia, I.; Llobet, E.; Blackman, C.; Correig, X.; Vallejos, S. Micromachined Gas Sensors Based on Tungsten Oxide Nanoneedles Directly Integrated via Aerosol Assisted CVD. *Sens. Actuators, B* **2014**, *198*, 210–218.
- (13) Giebelhaus, I.; Varechikina, E.; Fischer, T.; Rumyantseva, M.; Ivanov, V.; Gaskov, A.; Morante, J. R.; Arbiol, J.; Tyrra, W.; Mathur, S. One-Dimensional CuO – SnO_2 p–n Heterojunctions for Enhanced Detection of H_2S . *J. Mater. Chem. A* **2013**, *1*, 11261–11268.
- (14) Pandey, S. K.; Kim, K. H.; Tang, K. T. A Review of Sensor-Based Methods for Monitoring Hydrogen Sulfide. *TrAC, Trends Anal. Chem.* **2012**, *32*, 87–99.
- (15) Kim, S. S.; Na, H. G.; Choi, S. W.; Kwak, D. S.; Kim, H. W. Novel Growth of CuO -Functionalized, Branched SnO_2 Nanowires and their Application to H_2S Sensors. *J. Phys. D: Appl. Phys.* **2012**, *45*, 205301.
- (16) Xiaoyuan, J.; Huijuan, L.; Xiaoming, Z. Catalytic Activity of CuO -Loaded $\text{TiO}_2/\gamma\text{-Al}_2\text{O}_3$ for NO Reduction by CO . *J. Mater. Sci.* **2008**, *43*, 6505–6512.
- (17) Woo, H. S.; Kwak, C. H.; Kim, I. D.; Lee, J. H. Selective, Sensitive, and Reversible H_2S Sensors Using Mo-Doped ZnO Nanowire Network Sensors. *J. Mater. Chem. A* **2014**, *2*, 6412–6418.
- (18) Gurlo, A. Nanosensors: Towards Morphological Control of Gas Sensing Activity. SnO_2 , In_2O_3 , ZnO and WO_3 Case Studies. *Nanoscale* **2011**, *3*, 154–165.
- (19) Shen, G.; Chen, D.; Chen, P.; Zhou, C. Vapor–Solid Growth of One-Dimensional Layer-Structured Gallium Sulfide Nanostructures. *ACS Nano* **2009**, *3*, 1115–1120.
- (20) Vallejos, S.; Umek, P.; Stoycheva, T.; Annanouch, F.; Llobet, E.; Correig, X.; De Marco, P.; Blackman, C. Single-Step deposition of Au- and Pt-Nanoparticle-Functionalized Tungsten Oxide Nanoneedles Synthesized via Aerosol-Assisted CVD, and used for Fabrication of Selective Gas Microsensor Arrays. *Adv. Funct. Mater.* **2013**, *23*, 1313–1322.
- (21) Riaz, A.; Jung, K.; Chang, W.; Shin, K.; Lee, J. Carbon-, Binder-, and Precious Metal-Free Cathodes for Non-Aqueous Lithium–Oxygen Batteries: Nanoflake-Decorated Nanoneedle Oxide Arrays. *ACS Appl. Mater. Interfaces* **2014**, *6*, 17815–17822.
- (22) Kolmakov, A.; Klenov, D. O.; Lilach, Y.; Stemmer, S.; Moskovits, M. Enhanced Gas Sensing by Individual SnO_2 Nanowires and Nanobelts Functionalized with Pd Catalyst Particles. *Nano Lett.* **2005**, *5*, 4667–4673.
- (23) Van, P. T. H.; Thanh, N. H.; Quang, V. V.; Duy, N. V.; Hoa, N. D.; Hieu, N. V. Scalable Fabrication of High-Performance NO_2 Gas Sensors Based on Tungsten Oxide Nanowires by On-Chip Growth and RuO_2 -Functionalization. *ACS Appl. Mater. Interfaces* **2014**, *6*, 12022–12030.
- (24) Annanouch, F. E.; Stoycheva, T.; Vallejos, S.; Blackman, C.; Correig, X.; Llobet, E. AA-CVD Growth and Ethanol Sensing Properties of Pure and Metal Decorated WO_3 Nanoneedles. *Int. J. Nanotechnol.* **2013**, *10*, 455–469.
- (25) Vallejos, S.; Stoycheva, T.; Umek, P.; Navio, C.; Snyders, R.; Bittencourt, C.; Llobet, E.; Blackman, C.; Moniz, S.; Correig, X. Au Nanoparticle-Functionalised WO_3 Nanoneedles and their Application in High Sensitivity Gas Sensor Devices. *Chem. Commun. (Cambridge, U. K.)* **2011**, *47*, S65–S67.
- (26) Zanolli, Z.; Leghrib, R.; Felten, A.; Pireaux, J.; Llobet, E.; Charlier, J. Gas Sensing with Au-Decorated Carbon Nanotubes. *ACS Nano* **2011**, *5*, 4592–4599.
- (27) Palgrave, R. G.; Parkin, I. P. Aerosol Assisted Chemical Vapor Deposition Using Nanoparticle Precursors: A Route to Nanocomposite. *J. Am. Chem. Soc.* **2006**, *128*, 1587–1597.
- (28) Hill, M. S.; Johnson, A. L.; Manning, T. D.; Molloy, K. C.; Wickham, B. J. Single-Source AACVD of Composite Cobalt–Silicon Oxide Thin Films. *Inorg. Chim. Acta* **2014**, *422*, 47–56.
- (29) Shao, F.; Hoffmann, M. W. G.; Prades, J. D.; Zamania, R.; Arbiol, J.; Morante, J. R.; Varechikina, E.; Rumyantseva, M.; Gaskov, A.; Giebelhaus, I.; Fischer, T.; Mathur, S.; Hernández-Ramírez, F. Heterostructured p-CuO (Nanoparticle)/n- SnO_2 (Nanowire) Devices for Selective H_2S Detection. *Sens. Actuators, B* **2013**, *181*, 130–135.
- (30) Sun, G. J.; Choi, S. W.; Katoch, A.; Wu, P.; Kim, S. S. Bi-Functional Mechanism of H_2S Detection Using CuO – SnO_2 Nanowires. *J. Mater. Chem. C* **2013**, *1*, S454–S462.
- (31) Wang, C.; Chu, X.; Wu, M. Detection of H_2S Down to ppb Levels at Room Temperature Using Sensors Based on ZnO Nanorods. *Sens. Actuators, B* **2006**, *113*, 320–323.
- (32) Annanouch, F. E.; Vallejos, S.; Stoycheva, T.; Blackman, C.; Llobet, E. Aerosol Assisted Chemical Vapour Deposition of Gas-Sensitive Nanomaterials. *Thin Solid Films* **2013**, *548*, 703–709.
- (33) Annanouch, F. E.; Camara, M.; Ramírez, J. L.; Briand, D.; Llobet, E. Gas Sensing Properties of Metal-Decorated Tungsten Oxide Nanowires Directly Grown onto Flexible Polymeric Hotplates. *Procedia Eng.* **2014**, *87*, 700–703.
- (34) Vallejos, S.; Umek, P.; Blackman, C. Aerosol Assisted Chemical Vapour Deposition Control Parameters for Selective Deposition of Tungsten Oxide Nanostructures. *J. Nanosci. Nanotechnol.* **2011**, *11*, 8214–8220.
- (35) Navio, C.; Vallejos, S.; Stoycheva, T.; Llobet, E.; Correig, X.; Snyders, R.; Blackman, C.; Umek, P.; Ke, X.; Tendeloo, G. V.; Bittencourt, C. Gold Clusters on WO_3 Nanoneedles Grown via AACVD: XPS and TEM Studies. *Mater. Chem. Phys.* **2012**, *134*, 809–813.
- (36) Xie, F. Y.; Gong, L.; Liu, X.; Tao, Y. T.; Zhang, W. H.; Chen, S. H.; Meng, H.; Chen, J. XPS Studies on Surface Reduction of Tungsten Oxide Nanowire Film by Ar^+ Bombardment. *J. Electron Spectrosc. Relat. Phenom.* **2012**, *185*, 112–118.
- (37) Ottaviano, L.; Bussolotti, F.; Lozzi, L.; Passacantando, M.; La Rosa, S.; Santucci, S. Core Level and Valence Band Investigation of WO_3 Thin Films with Synchrotron Radiation. *Thin Solid Films* **2003**, *436*, 9–16.
- (38) Bussolotti, F.; Lozzi, L.; Passacantando, M.; La Rosa, S.; Santucci, S.; Ottaviano, L. Surface Electronic Properties of Polycrystalline WO_3 Thin Films: A Study by Core Level and Valence Band Photoemission. *Surf. Sci.* **2003**, *538*, 113–123.
- (39) Leftheriotis, G.; Papaefthimiou, S.; Yannoulis, P.; Siokou, A. Effect of the Tungsten Oxidation States in the Thermal Coloration and Bleaching of Amorphous WO_3 Films. *Thin Solid Films* **2001**, *384*, 298–306.
- (40) Wong, H. Y.; Ong, C. W.; Kwok, R. W.; Wong, K. W.; Wong, S. P.; Cheung, W. Y. Effects of Ion Beam Bombardment on Electrochromic Tungsten Oxide Films Studied by X-Ray Photoelectron Spectroscopy and Rutherford Back-Scattering. *Thin Solid Films* **2000**, *376*, 131–139.
- (41) Gurevich, A. B.; Bent, B. E.; Teplakov, A. V.; Chen, J. G. A NEXAFS Investigation of the Formation and Decomposition of CuO and Cu_2O Thin Films on $\text{Cu}(100)$. *Surf. Sci.* **1999**, *442*, L971–L976.
- (42) Grioni, M.; Goedkoop, J. B.; Schoorl, R.; De Groot, F. M. F.; Fuggle, J. C.; Schäfers, F.; Koch, E. E.; Rossi, G.; Esteve, J. M.;

Karnatak, R. C. Studies of Copper Valence States with Cu L3 X-Ray-Absorption Spectroscopy. *Phys. Rev. B: Condens. Matter Mater. Phys.* **1989**, *39*, 1541–1545.

(43) Bai, S.; Zhang, K.; Luo, R.; Li, D.; Chena, A.; Liu, C. C. Low-Temperature Hydrothermal Synthesis of WO₃ Nanorods and their Sensing Properties for NO₂. *J. Mater. Chem.* **2012**, *22*, 12643–12650.

(44) Song, P.; Han, D.; Zhang, H.; Li, J.; Yang, Z.; Wang, Q. Hydrothermal Synthesis of Porous In₂O₃ Nanospheres with Superior Ethanol Sensing Properties. *Sens. Actuators, B* **2014**, *196*, 434–439.

(45) Tong, P. V.; Hoa, N. D.; Quang, V. V.; Duy, N. V.; Hieu, N. V. Diameter Controlled Synthesis of Tungsten Oxide Nanorod Bundles for Highly Sensitive NO₂ Gas Sensors. *Sens. Actuators, B* **2013**, *183*, 372–380.

(46) EU, D. 50/EC of the European Parliament and of the Council of 21 May 2008 on Ambient Air Quality and Cleaner Air for Europe. *Off. J. Eur. Communities: Legis.* **2008**, L152.

(47) Wang, L.; Kang, Y.; Wang, Y.; Zhu, B.; Zhang, S.; Huang, W.; Wang, S. CuO Nanoparticle Decorated ZnO Nanorod Sensor for Low-Temperature H₂S Detection. *Mater. Sci. Eng., C* **2012**, *32*, 2079–2085.

(48) Galtayries, A.; Bonnelle, J. P. XPS and ISS Studies on the Interaction of H₂S with Polycrystalline Cu, Cu₂O and CuO Surfaces. *Surf. Interface Anal.* **1995**, *23*, 171–179.

(49) Bai, Z.; Xie, C.; Hu, M.; Zhang, S.; Zeng, D. Effect of Humidity on the Gas Sensing Property of the Tetrapod-Shaped ZnO Nanopowder Sensor. *Mater. Sci. Eng., B* **2008**, *149*, 12–17.

(50) Merdrignac-Conanec, O.; Bernicot, Y.; Guyader, J. Humidity Effect on Baseline Conductance and H₂S Sensitivity of Cadmium Germanium Oxynitride Thick Film Gas Sensors. *Sens. Actuators, B* **2000**, *63*, 86–90.

(51) Choi, K.; Kim, H.; Kang, Y. C.; Lee, J. Ultrasensitive and Ultrasensitive Detection of H₂S in Highly Humid Atmosphere Using CuO-Loaded SnO₂ Hollow Spheres for Real-Time Diagnosis of Halitosis. *Sens. Actuators, B* **2014**, *194*, 371–376.

(52) Barsan, N.; Weimar, U. Understanding the Fundamental Principles of Metal Oxide Based Gas Sensors; the Example of CO Sensing with SnO₂ Sensors in the Presence of Humidity. *J. Phys.: Condens. Matter.* **2003**, *15*, 813–839.

(53) Guttman, P.; Bittencourt, C.; Rehbein, S.; Umek, P.; Ke, X.; Tendeloo, G. V.; Ewels, C. P.; Schneider, G. Nanoscale Spectroscopy with Polarized X-Rays by NEXAFS-TXM. *Nat. Photonics* **2011**, *6*, 25–29.

(54) Krylova, V.; Andrulevicius, M. Optical, XPS and XRD Studies of Semiconducting Copper Sulfide Layers on a Polyamide Film. *Int. J. Photoenergy* **2009**, DOI: 10.1155/2009/304308.

(55) Strohmeier, B. R.; Leyden, D. E.; Field, R. S.; Hercules, D. M. Surface Spectroscopic Characterization of Cu/Al₂O₃ Catalysts. *J. Catal.* **1985**, *94*, 514–530.

(56) Selopala, G. S.; Concina, I.; Milana, R.; Natileb, M. M.; Sberveglieria, G.; Vomiero, A. Hierarchical Self-assembled Cu₂S Nanostructures: Fast and Reproducible Spray Deposition of Effective Counter Electrodes for High Efficiency Quantum Dot Solar Cells. *Nano Energy* **2014**, *6*, 200–210.

(57) Kundu, M.; Hasegawa, T.; Terabe, K.; Yamamoto, K.; Aono, M. Structural Studies of Copper Sulfide Films: Effect of Ambient Atmosphere. *Sci. Technol. Adv. Mater.* **2008**, DOI: 10.1088/1468-6996/9/3/035011.